






Microphase versus macrophase separation in the square-well-linear fluid: A theoretical and computational study

Dino Costa ¹, Gianmarco Munaò ^{1,*}, Jean-Marc Bomont ², Gianpietro Malescio,¹
Amedeo Palatella ³ and Santi Prestipino ¹

¹*Dipartimento di Scienze Matematiche e Informatiche, Scienze Fisiche e Scienze della Terra,
Università degli Studi di Messina, Viale F. Stagno d'Alcontres 31, 98166 Messina, Italy*

²*Université de Lorraine, LCP-A2MC, EA 3469, 1 Bd. François Arago, Metz F-57078, France*

³*Liceo Classico, Scientifico e delle Scienze Umane “Bonaventura Cavalieri”, Via Madonna di Campagna 18, 28922 Verbania, Italy*



(Received 26 June 2023; accepted 10 August 2023; published 6 September 2023)

Due to the presence of competing interactions, the square-well-linear fluid can exhibit either liquid-vapor equilibrium (macrophase separation) or clustering (microphase separation). Here we address the issue of determining the boundary between these two regimes, i.e., the Lifshitz point, expressed in terms of a relationship between the parameters of the model. To this aim, we carry out Monte Carlo simulations to compute the structure factor of the fluid, whose behavior at low wave vectors accurately captures the tendency of the fluid to form aggregates or, alternatively, to phase separate. Specifically, for a number of different combinations of attraction and repulsion ranges, we make the system go across the Lifshitz point by increasing the strength of the repulsion. We use simulation results to benchmark the performance of two theories of fluids, namely, the hypernetted chain (HNC) equation and the analytically solvable random phase approximation (RPA); in particular, the RPA theory is applied with two different prescriptions as for the direct correlation function inside the core. Overall, the HNC theory proves to be an appropriate tool to characterize the fluid structure and the low-wave-vector behavior of the structure factor is consistent with the threshold between microphase and macrophase separation established through simulation. The structural predictions of the RPA theory turn out to be less accurate, but this theory offers the advantage of providing an analytical expression of the Lifshitz point. Compared to simulation, both RPA schemes predict a Lifshitz point that falls within the macrophase-separation region of parameters: in the best case, barriers roughly twice higher than predicted are required to attain clustering conditions.

DOI: [10.1103/PhysRevE.108.034602](https://doi.org/10.1103/PhysRevE.108.034602)

I. INTRODUCTION

Model potentials featuring a short-range attraction (SA) and a long-range repulsion (LR) are commonly used to describe, under appropriate physicochemical conditions, the behavior of a large variety of soft materials, including colloidal suspensions, globular protein solutions, and polymers: just to quote a few illustrative examples, see [1–10]. Perhaps, the most intriguing feature of SALR fluids lies in the ability to spontaneously self-assemble into aggregates of various morphologies; this peculiar property stems from the competition between attractive and repulsive forces which, on the one side (SA), promote aggregation while, on the other side (LR), discourage macrophase (liquid-vapor) separation [11]. A number of recent reviews extensively account for both general and specific aspects of the physics of SALR models, witnessing at the same time the wide interest in these systems [12–16]. Mixtures containing SALR particles are more recently addressed in the literature [17–21].

At the structural level, an unambiguous signature of mesoscale inhomogeneities developing in the fluid is given by a peak in the structure factor $S(q)$ at a wave vector $q_p \neq 0$

well below the location of the main scattering peak [22,23], signaling the propensity of the system to form aggregates on a length scale $\approx 2\pi/q_p$. The height of the low- q peak eventually diverges upon approaching thermodynamic conditions where the density modulation becomes periodic (periodic microphases) [24]. On the other hand, when the competition between attraction and repulsion is unbalanced in favor of the former, a SALR fluid behaves like a simple fluid, exhibiting liquid-vapor equilibrium. In this case, as one enters the region of liquid-vapor coexistence, $S(q)$ diverges at $q = 0$ [25]. The locus separating the two scenarios is the Lifshitz point, i.e., a threshold in the space of model parameters across which the location of the divergent structure factor changes from 0 to a $q_p \neq 0$.

Until recently, many efforts have been devoted to determine, based on purely structural indicators, the threshold where a SALR fluid characterized by small local inhomogeneities, a condition generically termed “intermediate-range order” (IRO) in Ref. [5], evolves into a genuine cluster fluid, i.e., a situation marked by the presence of compact, relatively large (compared to the particle size) and weakly interacting aggregates, suspended in a sea of substantially smaller aggregates and isolated particles. The currently accredited view is that clusters form under the same thermodynamic conditions for which the attractive “reference” potential (obtained from

*Corresponding author: gianmarco.munao@unime.it

the full SALR interaction by cutting out the LR component) would exhibit liquid-vapor separation [26–28]. A simple, well verified, heuristic criterion states that the crossover from IRO to clustering is reached as $S(q_p)$ overcomes ≈ 2.7 [27,28], an indication in appealing analogy with the Hansen-Verlet criterion of freezing for simple fluids [29]. Other criteria, based on the width of $S(q_p)$ [30,31] or the long-range behavior of the radial distribution function [32–34], were proposed (see [16] for a review).

Even though simulation studies play a prominent role in the field, integral equation theories of fluids (IET) [35–37] are also a valuable tool. Indeed, the characterization of spatially inhomogeneous states in terms of the structure factor naturally fits within the scope of IET; moreover, SALR potentials extending over long distances can be studied by IET with much less computational cost than computer simulations. IET studies of SALR fluids employed from simple closures and semianalytical schemes [5,31,38–43] to sophisticated, thermodynamically self-consistent approaches [11,34,43–53]. With reference to this study, the HNC closure has been fruitfully employed in [40,43,54–56]. All these works demonstrate that IET can provide accurate structural and thermodynamic predictions. The even simpler RPA closure (and the closely related mean spherical approximation), aside from providing analytical expressions for the structure of the fluid, also offers the advantage that the Lifshitz point of various SALR potentials can be determined analytically [11,24,38]. Recently, a simple RPA expression for the Helmholtz free energy density functional of a two-Yukawa fluid has been used as an input for the first application of the nonequilibrium self-consistent generalized Langevin equation theory [57] to the description of dynamical arrest in a SALR model [58].

Many current studies concern a prototypical SALR model consisting of hard spheres interacting via the sum of two Yukawa potentials of opposite signs; another commonly used model is one in which the hard-core repulsion and the attractive Yukawa terms are replaced by a m - n Lennard-Jones-type interaction; other SALR models were comparatively less investigated (see [14–16]). A yet different model, which is attracting growing interest, is given by hard spheres interacting via an attractive square-well potential, followed by a linearly-descending ramp (SWLR hereafter). As far as we know, such a “square-well-linear” potential was originally proposed in 2009 by Cates and his group [59] to demonstrate that the combination of a short-range attraction with a repulsive barrier can strongly stabilize a particular kind of gel in which colloidal particles in a single-phase solvent have locally planar coordination. In a 2015 paper [56] we proposed the SWLR model as a convenient model of competing interactions. Even though rather schematic, the SWLR model offers the advantage that all three interaction parameters, namely, the width of the attraction, together with the height and range of the repulsive barrier, can be tuned independently from each other. This allows to examine how each parameter separately affects the overall behavior of the model and the aggregation process.

In Ref. [56] we focused on the thermodynamic conditions under which the fluid changes from homogeneous to slightly inhomogeneous, i.e., at the onset of the low- q peak. Therein, we documented a neatly linear increase of the temperature at

which IRO first appears (at constant density) as a function of either the square-well width or the height of the repulsive barrier; instead, we found a much stronger dependence on the repulsion range. Moreover, the typical distance between aggregates was shown to fall at an approximately fixed fraction of the width of the repulsive barrier. Immediately after, Charbonneau and coworkers analyzed in a series of papers [24,60–62] several other aspects of SWLR fluids, including a study of the disordered regime in one dimension [62]: in Ref. [60] the equilibrium phase diagram of a specific SWLR model was worked out, elucidating the thermodynamic interplay between cluster fluid, gel, and various periodic microphases. In Ref. [24], a specialized simulation method was employed to determine the phase behavior of the SWLR fluid for a couple of strengths and ranges of the repulsive component; theoretical predictions for microphase formation were shown to be in qualitative agreement with numerical results. In Ref. [61] the authors studied the dynamics of self-assembly at intermediate densities, identifying four different regimes and the structural changes that underlie the crossover from one regime to the next. Below the order-disorder transition line, they found that, among the periodic microphases, lamellae are the most easily accessible. More recently, by relying on the knowledge of the equilibrium phase behavior in the bulk [60], Gózdź and coworkers have studied a specific SWLR fluid under various confining geometries [63–66].

In this work we carry out an extended study of the structural properties of the SWLR model, in order to investigate the boundary between macrophase (liquid-vapor) and microphase (clustering) separation. Specifically, we use Monte Carlo (MC) simulations in the canonical ensemble to study three combinations of square-well and linear-ramp widths; in each case, the fluid is driven across the Lifshitz point by increasing the barrier height. To locate this threshold, all samples are gradually cooled at various fixed densities until, depending on the specific combination of interaction parameters, the fluid proceeds towards liquid-vapor separation or rather forms clusters. As discussed before, the different scenarios are distinguished based on the shape of the structure factor at low wave vectors. Simulations are complemented by hypernetted chain (HNC) and random phase approximation (RPA) calculations. In particular, within RPA we compare predictions obtained from the same direct correlation function employed in [24] with those obtained from a different prescription, corresponding to the bare Percus-Yevick solution for hard spheres in the core region [25].

Previous studies almost exclusively focused on a single value of the square-well width, taken to be half the hard-core diameter [24]. In this case, the purely attractive reference system essentially behaves like a simple fluid. Here, we also consider a very short-range attraction, where the square well extends for only a 2% of the core, so as to make the system akin to a colloidal fluid. We complete our survey with the intermediate case of a well width equal to 20% of the particle size.

The paper is organized as follows. In Sec. II we describe the SWLR model and introduce our RPA, HNC, and MC implementations. To facilitate the reading of results, the mathematical steps leading to the RPA expression of the structure factor are reported in Appendix A, while the ensuing Lifshitz

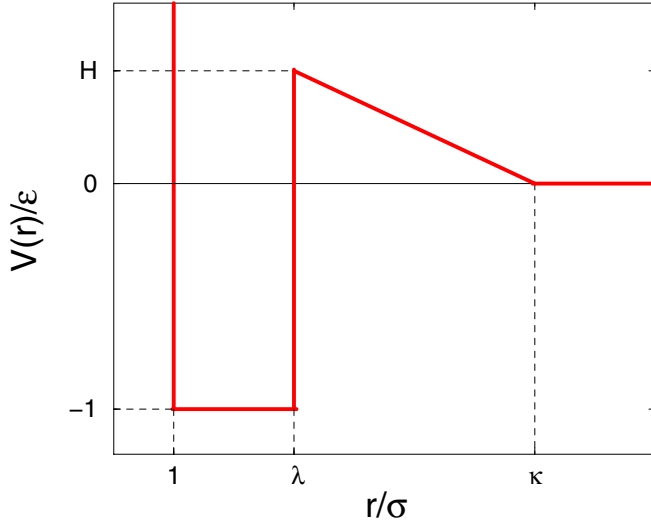


FIG. 1. The square-well-linear potential studied in this work [see Eq. (1)]. $H = \xi(\kappa - \lambda)$ indicates the top of the repulsive barrier at $r = \lambda\sigma$.

point is calculated in Appendix B. In Sec. III we make a survey of the HNC and RPA structural predictions, in comparison with Monte Carlo results. Section IV is devoted to the numerical determination of the Lifshitz point; this section is divided in three subsections, each one relative to a specific combination of square-well and linear-ramp widths. Section V is devoted to conclusions.

II. MODEL AND METHODS

Using the same notation of Ref. [24], the SWLR fluid consists of hard spheres of diameter σ interacting via an attractive square well (SW) of depth ε and width $(\lambda - 1)\sigma$, followed by a repulsive barrier in the form of a linearly descending ramp (LR), from a height $H = \xi(\kappa - \lambda)$ at $r = \lambda\sigma$ to zero at $r = \kappa\sigma$ (see Fig. 1). Outside the hard core, the interaction potential is then given by

$$\frac{V_{\text{SWLR}}(r)}{\varepsilon} = \begin{cases} -1, & \sigma \leq r < \lambda\sigma \\ \xi(\kappa - r), & \lambda\sigma \leq r < \kappa\sigma \\ 0, & \text{otherwise.} \end{cases} \quad (1)$$

From now on, distances will be expressed in units of σ and energies in units of ε ; accordingly, the density ρ is given in units of σ^{-3} and the temperature T in units of ε/k_B , k_B being the Boltzmann constant.

From the Ornstein-Zernike relation,

$$h(q) = \frac{c(q)}{1 - \rho c(q)}, \quad (2)$$

connecting the Fourier transforms of the direct and total correlation functions $c(r)$ and $h(r)$, the structure factor $S(q)$ follows as

$$S(q) = 1 + \rho h(q) = \frac{1}{1 - \rho c(q)}. \quad (3)$$

The radial distribution function is $g(r) = 1 + h(r)$.

In the RPA theory an approximate expression for $c(r)$ outside the core is obtained by extending to finite distances

the exact asymptotic behavior, given by $c(r) = -\beta V_{\text{SWLR}}(r)$, while various expressions were considered within the core (see, e.g., [24,38,42,45,67]). Here we choose the Percus-Yevick solution for the hard-sphere fluid $c_{\text{HS}}(r)$ [25]. In formulas

$$c(r) = \begin{cases} c_{\text{HS}}(r), & r < 1 \\ -\beta V_{\text{SWLR}}(r), & \text{otherwise} \end{cases} \quad (4)$$

where $\beta = 1/k_B T$. A second option, adopted by Zhuang and Charbonneau (ZC) [24] and also considered in this work, consists in adding another contribution to $c_{\text{HS}}(r)$, obtained by extending the definition of $V_{\text{SWLR}}(r)$ to $r < 1$ as $V_{\text{SWLR}}(r) = -\varepsilon$. For the model at issue, Eq. (4) is therefore rewritten as

$$c(r) = c_{\text{HS}}(r) - \beta V_{\text{SWLR}}(r), \quad (5)$$

independently of the distance r [notice that $c_{\text{HS}}(r) = 0$ outside the core]. For the sake of clarity, the two different schemes of Eqs. (4) and (5) will be hereafter referred to as RPA-PY and RPA-ZC, respectively. Within either of these schemes, the structure factor is analytical and derived in Appendix A. The RPA, with further simplifications valid in the low- q regime, also offers the opportunity to obtain the Lifshitz point in closed form (see Appendix B).

The HNC closure provides a more refined expression for $c(r)$, given by

$$c(r) = \exp[-\beta V(r) + \gamma(r)] - \gamma(r) - 1 \quad (6)$$

in terms of the indirect correlation function $\gamma(r) = h(r) - c(r)$. We numerically solve the coupled set of Eqs. (2) and (6) via a Picard iteration, with standard mixing of the $\gamma(r)$ functions at successive iterations. We assume that convergence is achieved when two successive estimates of $c(r)$ are equal to within 10^{-9} . Calculations are carried out on a grid of 2^{17} points with a mesh in real space of resolution $\Delta r/\sigma = 5 \times 10^{-4}$, thus covering a maximum distance of $r_{\text{max}} \approx 65\sigma$, with an ensuing minimum q value equal to $\Delta q = \pi/r_{\text{max}} \approx 0.0479$. We resort to such a fine mesh to ensure an accurate “sampling” of distances near the discontinuities in $V(r)$, as well as inside the attractive square well, which is especially necessary for the smallest value of λ considered here.

Canonical ensemble (NVT) Monte Carlo simulations are carried out on a sample of 1024 particles, enclosed in a cubic box with periodic boundary conditions. For the cases examined in Sec. III, where one or two thermodynamic conditions are analyzed for any given combination of SWLR parameters, we have employed a larger sample of $N = 4096$ particles. Production runs range from 2×10^6 to 1×10^7 MC cycles, depending on thermodynamic conditions; each run is divided in blocks of 500 000 cycles, so as to ensure small statistical uncertainties. As a standard improvement to the Metropolis algorithm, especially appropriate in the case of inhomogeneous configurations, at each MC step we randomly choose between two values of the maximum random displacement. The MC structure factors presented throughout the paper are computed from the correlation between density fluctuations [25]; we have verified in a number of cases that results agree with the calculation of $S(q)$ carried out in terms of the Fourier transform of $h(r)$.

TABLE I. The combinations of $[\lambda, \kappa, \xi]$ parameters analyzed in this work; the height of the repulsive barrier $H = \xi(\kappa - \lambda)$ is also reported for completeness. In the last column, for each model we indicate the relative figures in the text.

$[\lambda, \kappa]$	ξ	H	Figure
[1.02, 5.0]	2×10^{-5}	7.96×10^{-5}	5(a)
	2×10^{-4}	7.96×10^{-4}	5(b), 7(a)
	2×10^{-3}	7.96×10^{-3}	5(c), 7(b)
	1×10^{-2}	0.0398	5(d)
	0.0754	0.30	2, top
[1.2, 3.0]	0.0100	0.018	8
	0.0150	0.027	8
	0.0250	0.045	8
	0.0500	0.09	8
[1.5, 4.0]	0.0050	0.0125	3
	0.0200	0.05	9
	0.0300	0.05	2, bottom

III. RPA AND HNC PREDICTIONS FOR THE FLUID STRUCTURE

We have investigated the structure of the SWLR fluid for three pairs of $[\lambda, \kappa]$ parameters, namely, [1.02, 5.0], [1.2, 3.0], and [1.5, 4.0], and for several values of ξ , chosen so as to encompass the Lifshitz point for each $[\lambda, \kappa]$ pair (see Sec. IV). These cases are reported in Table I, where, for each $[\lambda, \kappa, \xi]$ combination, we also indicate in the last column the relative figure(s) in the text. In Table 1 of their recent paper [14], Liu and Xi introduced a broad categorization of the experimental and theoretical studies of SALR potentials up to date, identifying three different classes with distinctive phase diagrams, structures, and dynamics. Our choice of SWLR parameters naturally fits within this classification; specifically, the models with $\lambda = 1.02$ and $\lambda = 1.2$ fall within type-II category (SALR potentials with attraction range substantially shorter than the particle size and repulsion range comparable or larger than that) whereas the model with $\lambda = 1.5$ belongs to the type-III class (attraction larger than 20% of the particle size but still shorter than the repulsion range).

In Fig. 2 we make a first assessment of the RPA and HNC theories against MC data for two sets of parameters. In both cases, the presence of a low- q peak in the structure factor (left panels) that quickly rises on cooling is a clear signal of microphase separation. In the left panels we observe that the HNC theory (blue lines) correctly reproduces the MC structure factor (circles), even in cases where the fluid is presumably clustered. This occurs at $T = 0.40$ for $\lambda = 1.02$ [Fig. 2(b)] and at $T = 0.72$ for $\lambda = 1.5$ [Fig. 2(f)], where in fact $S(q_p)$ is well above the threshold ≈ 2.7 for the onset of clustering [27,28]. On the other hand, both RPA schemes are less accurate overall, with RPA-PY (red lines) underestimating $S(q_p)$, whereas RPA-ZC (green lines) overestimates it. Since theoretical schemes will eventually fail to converge when the first peak of the predicted structure factor becomes too high, RPA-ZC is unable to attain the low-temperature regime, which can instead be addressed by both HNC and RPA-PY. In the right panels of Fig. 2 we see that the HNC

theory accurately describes the local order in the fluid, as witnessed by the good agreement of $g(r)$ with MC data, even within the attractive well (see the insets). As for the RPA theory, $g(r)$ is obtained from the numerical Fourier transform of $S(q)$. In this case, the agreement with MC is poor and worsens at lower temperatures; moreover, unphysical negative values of $g(r)$ are found within the core.

In Fig. 3 we consider the same pair $[\lambda = 1.5, \kappa = 4]$ as in Figs. 2(e)–2(h), but we reduce ξ from 0.030 to 0.005. In this case, the repulsive barrier is not sufficient to promote clustering and liquid-vapor separation takes place instead, as signaled by the diverging trend of the MC $S(q \rightarrow 0)$ [Fig. 3(a)]. This specific SWLR fluid is studied for three densities, $\rho = 0.1, 0.3$, and 0.6 , at temperatures $T = 1.177, 1.218$, and 0.783 , respectively. These temperatures are the lowest limits attainable by the HNC theory at the given densities.

In Fig. 3(a) we confirm the accuracy of the HNC $S(q)$, except for the tendency of the theory to slightly underestimate $S(q \rightarrow 0)$ at high density. These discrepancies may be intrinsic to the HNC theory [68], but they could be in part due to the difficulty of estimating $S(q \rightarrow 0)$ by NVT simulations. As for the RPA theory, in parallel with the discussion of Fig. 2, RPA-PY gives a lower $S(0)$ in comparison with RPA-ZC, with the latter theory in better agreement with MC data, especially on the vapor side. Another issue actually affects RPA-PY predictions at high density: as is seen in Fig. 3(a) (red full line), the strong underestimation of $S(0)$ is accompanied by the presence of a large, cusplike main peak at $q\sigma \approx 2\pi$, which is totally absent in MC data; this feature ultimately triggers the failure of the RPA-PY analytical solution in this high-density, low-temperature regime.

In Fig. 3(b), similarly to what reported in Figs. 2(g) and 2(h), the HNC $g(r)$ turns out to be reasonably accurate. Some discrepancies with MC data only emerge within the attractive well: in particular, a little overestimation of density correlations at low density (black line) turns into an underestimation at high density (red line), with the best agreement in the intermediate case $\rho = 0.3$ (blue line), where HNC and MC results are practically coincident for all distances. The analysis of the RPA $g(r)$ does not add much to what discussed in relation to Fig. 2 and therefore we make no further comments on this.

To sum up after this preliminary analysis, the HNC theory is a reliable tool to determine the structural properties of the SWLR fluid, under both microphase- and macrophase-separation conditions. RPA predictions are poorer overall.

IV. RESULTS FOR THE LIFSHITZ POINT

In spite of the shortcomings just highlighted, it is worth considering the RPA theory here because of the possibility to derive the Lifshitz point analytically. This section is concerned with a detailed assessment of RPA predictions against MC results for the three $[\lambda, \kappa]$ pairs of Table I. Furthermore, the availability of fresh simulation data provides the occasion for a parallel validation of the HNC theory.

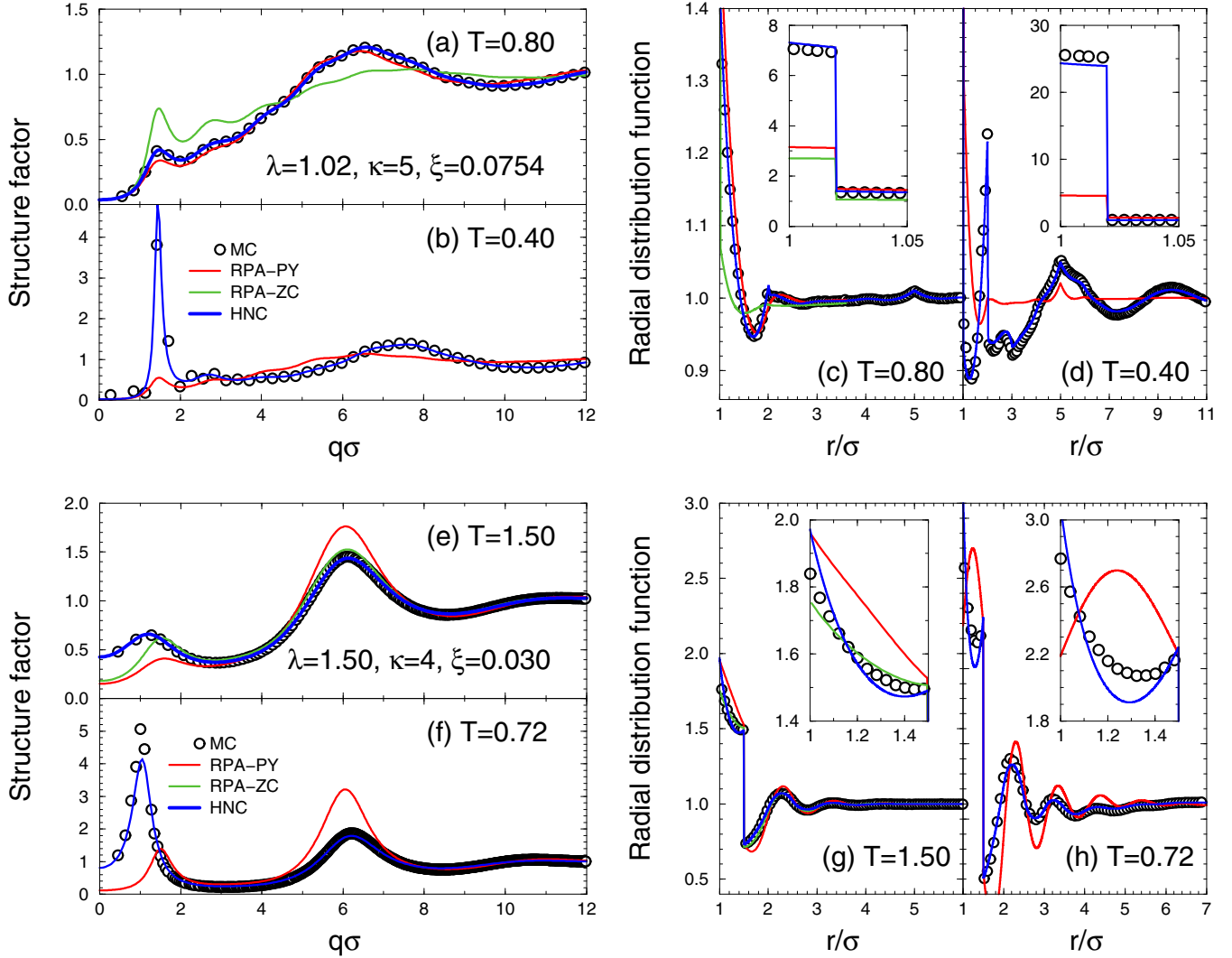


FIG. 2. Comparison between theoretical predictions (lines) and MC results (circles) for the structure of two SWLR models with $[\lambda, \kappa, \xi]$ combinations indicated in (a) (for top panels) and (e) (for bottom panels). All results are obtained for $\rho = 0.382$ (i.e., for a packing fraction $\eta = 0.20$), and temperatures indicated in each panel. The low-temperature cases $T = 0.40$ [(b) and (d)] and $T = 0.72$ [(f) and (h)] are beyond the reach of RPA-ZC and therefore no green lines are shown. A magnification of $g(r)$ within the attractive well is reported in the insets.

A. RPA predictions

As reported in Appendix B, the Lifshitz point (LP) of the SWLR fluid reads as

$$\xi_{\text{LP}}^{\text{PY}} = \frac{6(\lambda^5 - 1)}{\kappa^6 - 6\kappa\lambda^5 + 5\lambda^6} \quad \text{or} \quad \xi_{\text{LP}}^{\text{ZC}} = \frac{6\lambda^5}{\kappa^6 - 6\kappa\lambda^5 + 5\lambda^6}, \quad (7)$$

depending on the specific version of the RPA theory considered: as before, superscripts PY and ZC refer to the RPA-PY and RPA-ZC schemes, respectively. In Eq. (7) the Lifshitz point is expressed as a function of the attraction and repulsion widths, λ and κ , and is thus a surface $\xi_{\text{LP}}(\lambda, \kappa)$ in the $[\lambda, \kappa, \xi]$ space of SWLR parameters. Above this surface, i.e., for $\xi > \xi_{\text{LP}}$, the barrier is high enough for the SA vs LR competition to be effective in inducing microphase separation; on the other side of the surface, i.e., for $\xi < \xi_{\text{LP}}$, attraction dominates and liquid-vapor separation now takes place.

Interestingly, $\xi_{\text{LP}}^{\text{PY}}$ has the same expression as predicted in [24] from the structure of the ground state, which was calculated according to a low-temperature, low-density approximation of the interaction energy (LTA). Therefore, both RPA-PY and LTA theories lead to the same form of the Lifshitz point, despite the two routes start from quite different assumptions. As for $\xi_{\text{LP}}^{\text{ZC}}$, it corresponds to the same expression reported in [24]: both RPA-PY and RPA-ZC predictions will be discussed side by side in the rest of this section.

In Fig. 4 we show the behavior of $\xi_{\text{LP}}^{\text{PY}}$ (full lines) and $\xi_{\text{LP}}^{\text{ZC}}$ (dashed lines) as a function of κ for fixed $\lambda = 1.02, 1.2$, and 1.5 [Fig. 4(a)]. In Fig. 4(b), the same quantities are plotted as functions of λ for fixed $\kappa = 3, 4$, and 5 . The λ and κ ranges in the figure encompass the $[\lambda, \kappa]$ pairs reported in Table I. The numerical values of $\xi_{\text{LP}}^{\text{PY}}$ and $\xi_{\text{LP}}^{\text{ZC}}$ are reported in Table II; the corresponding MC estimates, to be presented below, are anticipated for a quick comparison in the last column of the same table. It is clear from Eq. (7) that $\xi_{\text{LP}}(\kappa)$ diverges as

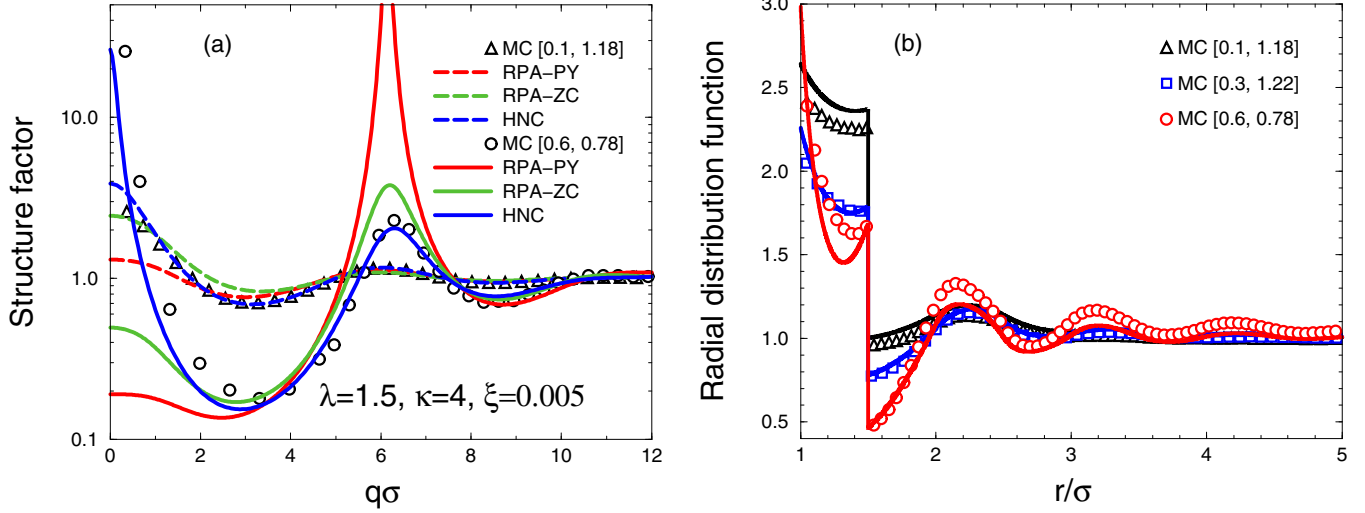


FIG. 3. Comparison between theoretical predictions (lines) and MC results (symbols) for the structure of the SWLR model with $[\lambda, \kappa, \xi]$ in (a) and $[\rho, T]$ in the legends. In (a), the correspondence is dashed lines vs triangles and full lines vs circles. In (b), only the comparison between MC and HNC is made; symbols and lines having the same color refer to the same ρ and T pairs. Results for $\rho = 0.3$ are omitted in (a) to avoid overcrowding.

$\kappa \rightarrow \lambda$: the narrower the repulsive barrier, the higher ξ must be in order to destabilize liquid-vapor separation in favor of clustering. At the opposite end, ξ_{LP} rapidly decreases with increasing κ : for fixed λ , in the range $\kappa = 2-5$ the value of ξ_{LP} drops by more than two orders of magnitude. Moreover, while the differences between ξ_{LP}^{PY} and ξ_{LP}^{ZC} are marginal for $\lambda = 1.5$, they become substantial for smaller λ : for instance, for $\lambda = 1.02$ differences of more than one order of magnitude arise between the two predictions (see Table II). Similarly, in Fig. 4(b) we see that, for fixed κ , ξ_{LP} must grow with λ in order to temper (in favor of clustering) the larger amount of attraction available from the square well. This growth is less and less pronounced as κ becomes progressively larger. In the inset we can appreciate how the difference between the two RPA estimates of ξ_{LP} shrinks as λ increases, independently of κ .

B. Narrow square well: $\lambda = 1.02, \kappa = 5$

Turning back to the comparison of theory with simulation, we first consider the case of a narrow square-well width, $\lambda = 1.02$ (with $\kappa = 5.0$), for which the two RPA schemes give largely different predictions for ξ_{LP} (see Table II). From the analysis of Fig. 2 (top panels), we already know that $\xi = 0.0754$ is a sufficiently large value to induce clustering; hence, this specific ξ is above ξ_{LP} . In the four panels of Fig. 5 we show the MC $S(q)$ for lower ξ values, namely, 0.2×10^{-4} (a), 0.2×10^{-3} (b), 0.2×10^{-2} (c), and 0.01 (d), encompassing the two different RPA predictions for ξ_{LP} . The MC data in Fig. 5 are relative to two densities, namely, a low value ($\rho = 0.1$, squares) and a high value ($\rho = 0.6$, circles), at various temperatures in the range $0.25-0.40$. In Fig. 6 we report two

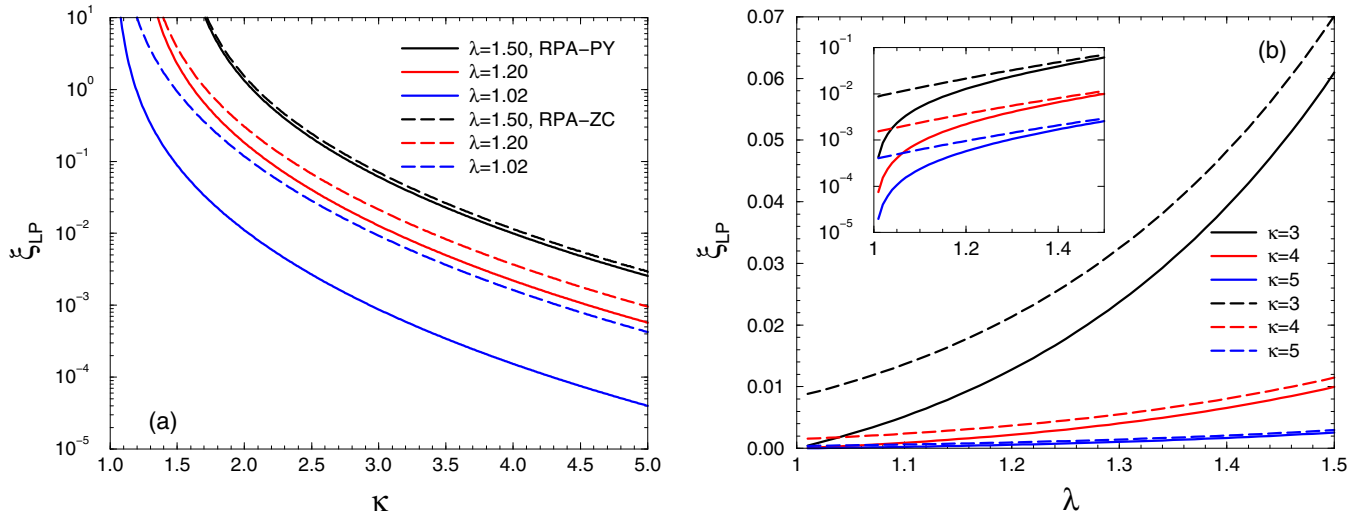


FIG. 4. RPA Lifshitz point expressed as $\xi_{LP}(\kappa)$ for fixed λ (a) and $\xi_{LP}(\lambda)$ for fixed κ (b) (see the legends). Solid and dashed lines, respectively, correspond to ξ_{LP}^{PY} and ξ_{LP}^{ZC} predictions [see Eq. (7)]. Inset: same as in the main panel, but for the logarithmic vertical scale.

TABLE II. RPA predictions for the Lifshitz points according to Eq. (7). MC results, $\xi_{\text{LP}}^{\text{MC}}$, are reported for comparison in the last column.

$[\lambda, \kappa]$	$\xi_{\text{LP}}^{\text{PY}}$	$\xi_{\text{LP}}^{\text{ZC}}$	$\xi_{\text{LP}}^{\text{MC}}$
[1.02, 5.0]	0.40×10^{-4}	0.42×10^{-3}	$[0.2\text{--}2] \times 10^{-3}$
[1.20, 3.0]	0.0128	0.0213	0.025–0.050
[1.50, 4.0]	0.996×10^{-2}	1.15×10^{-2}	0.02–0.03

snapshots of the low-density fluid with $\xi = 0.2 \times 10^{-4}$ and $\xi = 0.01$.

For the lowest ξ investigated [Fig. 5(a)], the behavior of $S(q)$ already heralds the divergence at $q = 0$ occurring at lower temperatures, i.e., macrophase separation. In Fig. 5(a) the temperatures considered are such that the system quickly reaches equilibrium. On slightly cooling the sample (for instance, going from $T = 0.260$ to $T = 0.258$ for $\rho = 0.1$), the decay to equilibrium becomes much slower, taking more that

4×10^7 MC cycles for the system to complete relaxation. The final system configuration is shown in Fig. 6(a). Here we see a very dilute vapor coexisting with a polycrystalline droplet, characterized by large ordered domains separated by grain boundaries. This indicates that, for the SWLR fluid at issue, the interparticle attraction is so short range that the available “glue” is insufficient to promote the stability of the liquid [69], implying that the vapor coexists with the solid. The behavior in Fig. 5(b) closely reflects that in Fig. 5(a), despite the fact that ξ has been increased by an order of magnitude.

The scenario illustrated in Figs. 5(c) and 5(d) is different: here we see that a low- q peak develops in both the dilute and the dense sample at $T = 0.30\text{--}0.40$, and further grows on cooling, pointing to the onset of a clustered state at lower temperatures. Comparing Figs. 5(c) and 5(d), we see that a higher repulsive barrier in Fig. 5(d), under the same temperature and density conditions, gives rise to a more refined and higher low- q peak, implying an earlier, i.e., occurring at higher temperatures, onset of clustering. Upon cooling the sample with $\rho = 0.1$ and $\xi = 0.01$ from $T = 0.25$ to 0.20 ,

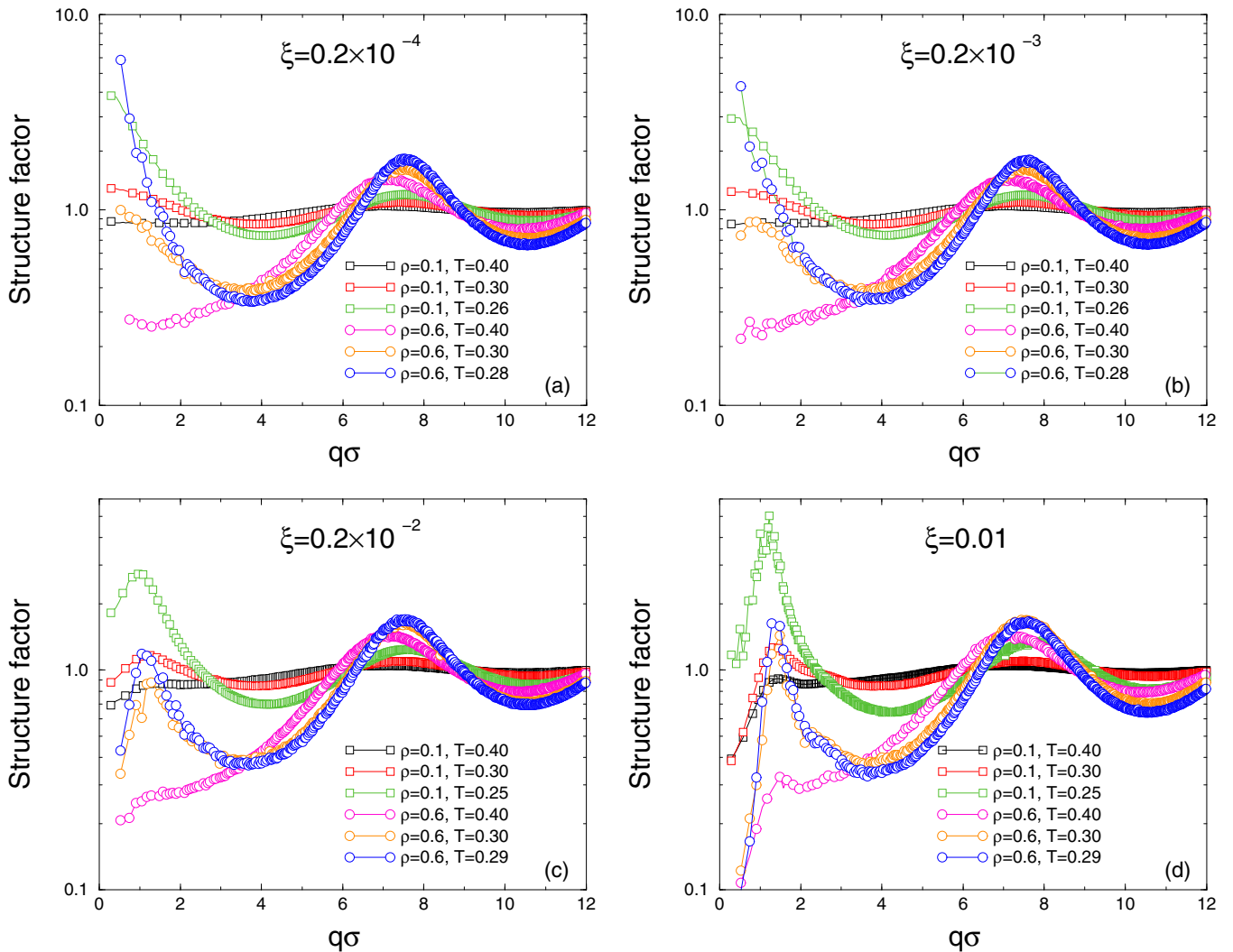


FIG. 5. MC structure factor for $[\lambda = 1.02, \kappa = 5]$ and four ξ , indicated in each panel. Two densities, $\rho = 0.1$ (squares) and $\rho = 0.6$ (circles), and several temperatures (in the legends) are analyzed.

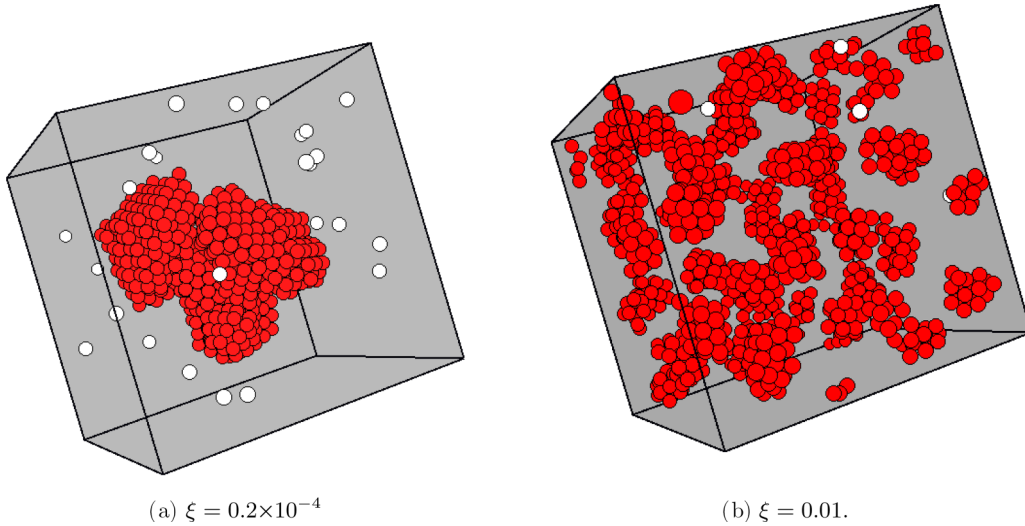


FIG. 6. Typical equilibrium configurations of the SWLR fluid with $[\lambda = 1.02, \kappa = 5]$, for $\xi = 0.2 \times 10^{-4}$ (a) and $\xi = 0.01$ (b). The thermodynamic conditions are $\rho = 0.1, T = 0.258$ (a) and $\rho = 0.1, T = 0.20$ (b). Isolated particles are drawn in white.

we obtain the well-defined clustered state shown in Fig. 6(b). The snapshots in Fig. 6 are only reported for the purpose of demonstrating that the typical equilibrium configuration of the system is coherent with the structural evidence shown in Fig. 5.

We point out that specifically tailored SALR models, determined via inverse-design optimization [70,71], are able to form porous mesophases, with a peculiar void-bubble structure. In common with the present SWLR interactions, these models share a narrow and deep attractive well, whereas the repulsive barrier shows more complex features, with a broader and shorter shape, in relation to standard cluster-forming interactions [see, for example, Fig. 1(b) of Ref. [70]]. As for the effect of the density, high- ρ values promote the formation of spherical and monodisperse voids, which self-organize into a periodic structure, whereas more mobile pores are observed over a large range of lower packing fractions [70]. Similar to our case, porous mesophases are expected to be separated from macrophase separation by a Lifshitz point [54]. Investigating whether specific SWLR models could give rise to similar self-assembled complex structures is an intriguing issue that may be addressed in future studies. As well, this would call for a detailed characterization in terms of the structure factor since the behavior of $S(q)$ should represent the primary source to identify such porous phases experimentally (and to distinguish them from other aggregate structures) in nanoscale colloids with similar interactions.

Turning back to Fig. 5, we deduce that ξ_{LP} for $[\lambda = 1.02, \kappa = 5]$ falls somewhere between 0.2×10^{-3} and 0.2×10^{-2} . Looking at Table II, it turns out that both RPA schemes provide a too low value of ξ_{LP} for the fluid to escape the liquid-vapor separation condition in favor of clustering. Therefore, the higher value of ξ_{LP} provided by RPA-ZC makes this theory more accurate than RPA-PY. Specifically, if we assume, in the absence of more information from MC, that $\xi_{LP} \approx 10^{-3}$, then ξ_{LP}^{ZC} is a factor of 2 to 3 smaller than the exact threshold.

The large set of MC data collected in Fig. 5 give us the opportunity to check the HNC structural predictions against

simulation. This task is accomplished in Fig. 7 for $\xi = 0.2 \times 10^{-3}$ (a) and $\xi = 0.2 \times 10^{-2}$ (b), close to the MC Lifshitz point [see Figs. 5(b) and 5(c)]. As is evident, the HNC theory correctly identifies the location of the crossover between liquid-vapor separation and clustering since in Fig. 7(a) we see an increase of $S(q \rightarrow 0)$, whereas in Fig. 7(b) we see the rising of a low- q peak. Within working conditions for the HNC theory, i.e., for temperatures not below $T \approx 0.26$ – 0.28 for the cases at issue, the theoretical predictions on the dilute side ($\rho = 0.1$, squares) turn out to be quantitative; on the liquid side, $\rho = 0.6$, the closer the “diverging” conditions [blue lines and circles in Figs. 7(a) and 7(b)], the less accurate the theory predictions. We have ascertained that the HNC theory improves when ξ is farther away from ξ_{LP} , e.g., for $\xi = 0.2 \times 10^{-4}$ or $\xi = 0.01$, corresponding to Figs. 5(a) and 5(d).

C. Intermediate square well: $\lambda = 1.2, \kappa = 3$

For the SWLR fluid with $[\lambda = 1.2, \kappa = 3]$, $\xi_{LP}^{PY} \approx 0.0128$ and $\xi_{LP}^{ZC} \approx 0.0213$ (see Table II). We explore by MC four ξ values around these thresholds, namely, $\xi = 0.010, 0.015, 0.025$, and 0.050 . Results are reported in Fig. 8(a); they are relative to $\rho = 0.2$, with temperatures in the range 0.40 – 0.60 . As far as ξ is less or equal to 0.025 (black, red, and blue lines), the structure factor shows a clear tendency to diverge at $q \rightarrow 0$. At fixed density and temperatures, the lower the repulsive barrier, the more marked this tendency. Clustering conditions are eventually established when the repulsive barrier is further increased, namely, for $\xi = 0.050$ (green lines), at which a low- q peak is evident in $S(q)$; this peak quickly increases from ≈ 2 to ≈ 10 as the system is cooled from $T = 0.55$ to 0.40 .

If we arbitrarily assume that the exact Lifshitz point falls halfway between $\xi = 0.025$ and 0.050 , the present analysis confirms that ξ_{LP}^{PY} falls inside the “simple-fluid behavior” region. However, compared to the case $[\lambda = 1.02, \kappa = 5]$ discussed before, the deviation from MC is now smaller. As

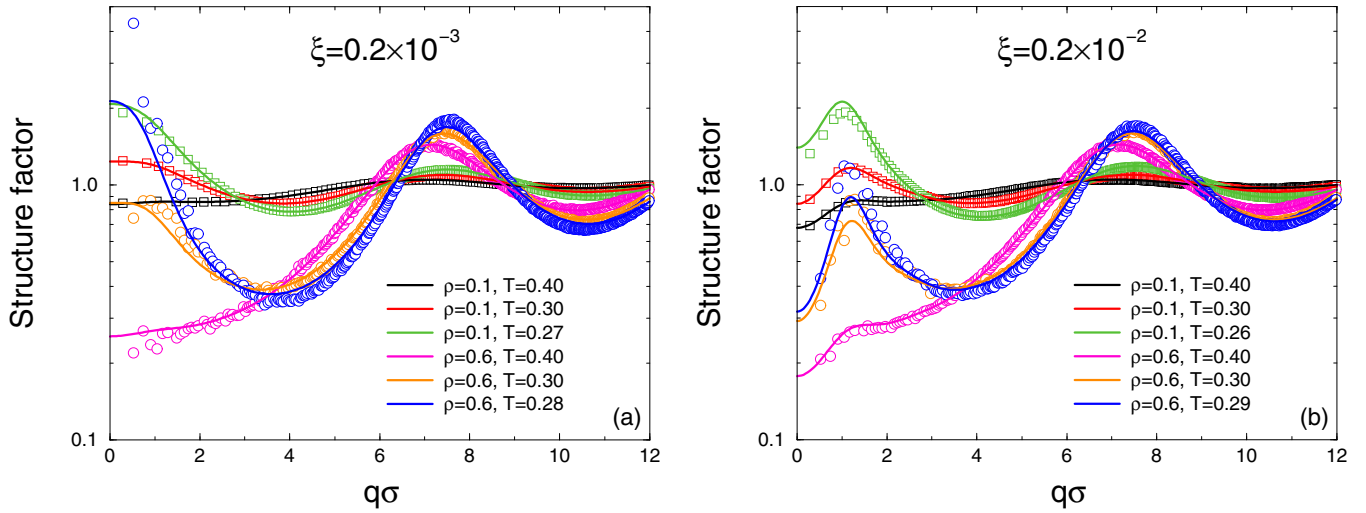


FIG. 7. Comparison between MC (symbols) and HNC (lines) structure factors for $[\lambda = 1.02, \kappa = 5]$ and two ξ , indicated in each panel. Squares: MC at $\rho = 0.1$; circles: MC at $\rho = 0.6$. Symbols and lines of same color refer to the same temperature, in the legends.

for RPA-ZC, we equally confirm that ξ_{LP}^{ZC} is two to three times smaller than the exact Lifshitz point.

As for the HNC predictions, a comparison with MC results is reported in Fig. 8(b). Again, the theory correctly predicts the threshold between microphase and macrophase separation; similarly to the previous cases, the overall shape of the structure factor is well reproduced in all situations, except for a mismatch occurring very close to $q = 0$ below the Lifshitz point.

D. Large square well: $\lambda = 1.5, \kappa = 4$

We complete our survey with the case $[\lambda = 1.5, \kappa = 4]$, for which we already know that the values $\xi = 0.005$ (Fig. 3) and $\xi = 0.030$ (Fig. 2) fall on opposite sides of the Lifshitz point. Also, in Table II we read $\xi_{LP}^{PY} \approx \xi_{LP}^{ZC} \approx 0.010$. For a more precise determination of the Lifshitz point, in Fig. 9 we examine the case $\xi = 0.020$, a value intermediate

between the RPA predictions and the Gibbs ensemble Monte Carlo estimate $\xi_{LP}^{GEMC} = 0.025 \pm 0.005$ [24]. In the figure, we plot the MC structure factor for a low ($\rho = 0.1$, (a)) and a high density ($\rho = 0.6$, (b)), at various temperatures. The fluid clearly exhibits a tendency to macrophase separation, as can be appreciated from the sharp increase of $S(q \rightarrow 0)$ on cooling, both on the vapor [Fig. 9(a)] and on the liquid [Fig. 9(b)] side. This finding is in agreement with the GEMC estimate and demonstrates the consistency between the thermodynamic and structural routes in the determination of the Lifshitz point. Again, doubling the value of ξ_{LP}^{ZC} gives a reasonable estimate of the exact Lifshitz point. As for the HNC predictions, the good accuracy observed in Figs. 2 and 3 for $[\lambda = 1.5, \kappa = 4]$ deserves no further examination.

A conclusive visual summary of our results is shown in Fig. 10. Therein we report the Lifshitz point calculated through both RPA-PY and RPA-ZC for the three $[\lambda, \kappa]$ pairs analyzed before. Alongside, the MC results for the occurrence

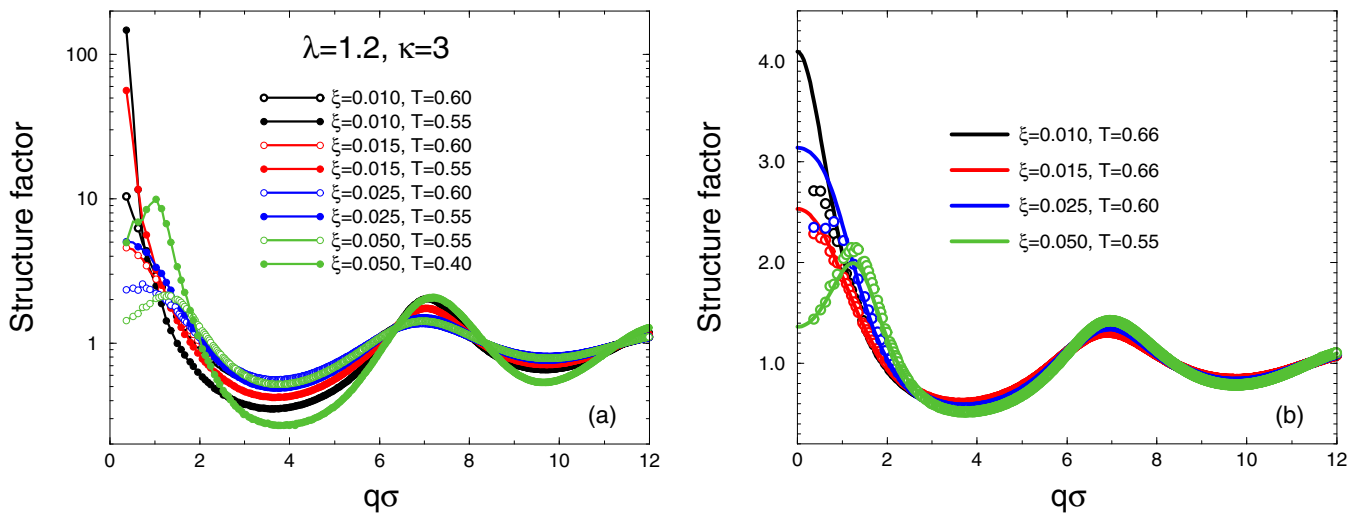


FIG. 8. (a) MC structure factor for $[\lambda, \kappa]$ indicated in (a) and various $[\xi, T]$ in the legend. The density is fixed at $\rho = 0.2$. (b) Comparison between MC (circles) and HNC (lines) for $[\xi, T]$ in the legend; symbols and lines of same color refer to the same $[\xi, T]$ conditions.

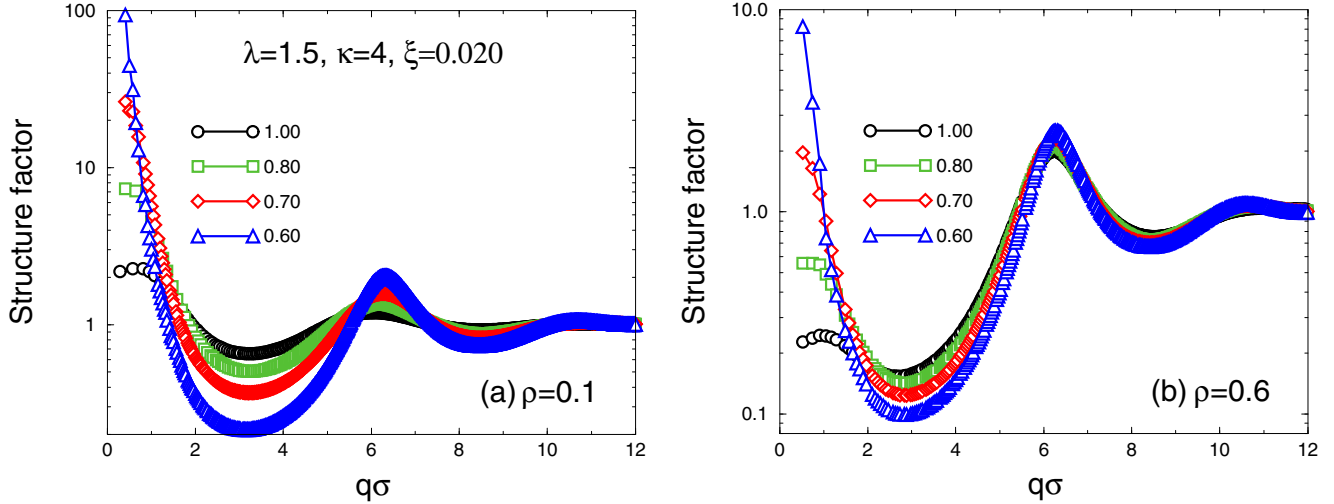


FIG. 9. MC structure factor for $[\lambda, \kappa, \xi]$ indicated in (a), at low $[\rho = 0.1, (a)]$ and high density $[\rho = 0.6, (b)]$, and for progressively lower temperatures, in the legends.

of either liquid-vapor separation or clustering are marked by squares and triangles, respectively. For the sake of comparison, we also report in the figure the GEMC result $\xi_{LP} = 0.025(5)$ for $\lambda = 1.5$ and $\kappa = 4$ [24], so as to document the perfect agreement between structural and thermodynamic indications.

V. CONCLUSIONS

Using extensive Monte Carlo simulations, we have investigated the structure of the square-well-linear fluid under thermodynamic conditions close to either liquid-vapor separation or clustering. To elucidate how the model parameters

distinguish between these two scenarios, we have analyzed three different sets of attraction and repulsion widths λ and κ , respectively, with $\lambda - 1$ ranging from 2% of the hard-core diameter σ (typical of colloidal solutions) to 0.5σ (typical of simple fluids), with the further intermediate case of 0.2σ . While keeping λ and κ fixed, we progressively increase the height of the repulsive barrier ξ until we observe the crossover from macrophase (liquid-vapor) separation to microphase separation (clustering). Our results are summarized in Fig. 10.

We have used simulations to assess the performance of a few integral equation theories of fluids. Specifically, we consider the hypernetted chain equation and the analytically solvable random phase approximation with two different prescriptions as for the form of the direct correlation function inside the core. The first case (named RPA-PY in the text) corresponds to the Percus-Yevick solution for hard spheres, whereas the second case (named RPA-ZC) is obtained by adding a constant term to the PY term, as provided by the backward extension of the square-well interaction to zero distance.

It turns out that HNC structural predictions agree well with MC data. This has been extensively verified for the variety of square wells analyzed here, and in particular in the case of an attraction width as short as 0.02σ . As well, the theory turns out to be accurate over a whole interval of reduced densities spanning the fluid regime, from $\rho = 0.1$ to 0.6 , also encompassing the putative critical region of reference fluids. Relevant to our study, the theory correctly reproduces those low-wave-vector features of the structure factor $S(q)$ that discriminate between microphase and macrophase separations. Small deviations from MC data are only seen in the height of the low- q peak of the structure factor (when the fluid is close to clustering) or in its $q = 0$ value (when liquid-vapor separation is approached instead). As expected for a theory designed to describe homogeneous fluids, the numerical algorithm fails to converge or provides unphysical results, typically manifesting in spurious negative values in $S(q)$ or unrealistically large and persistent oscillations in $g(r)$, as the low-temperature

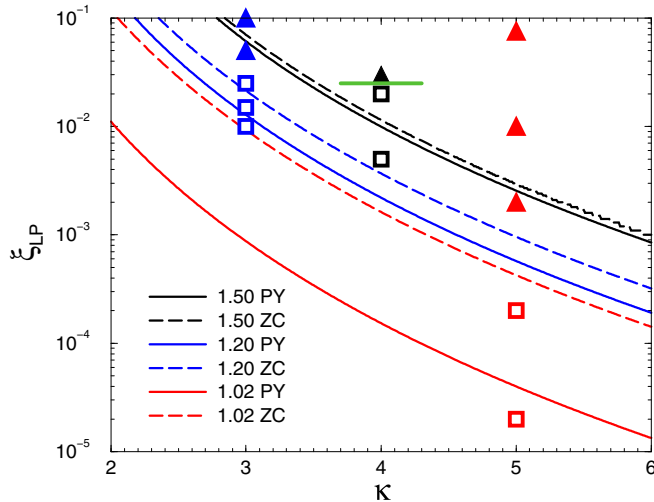


FIG. 10. The RPA Lifshitz points ξ_{LP}^{PY} (full lines) and ξ_{LP}^{ZC} (dashed lines) as functions of κ for the three λ values investigated in this work (in the legend). Symbols refer to MC results for those $[\lambda, \kappa, \xi]$ sets (same color, same λ) for which we have established that either liquid-vapor phase separation (squares) or clustering (triangles) takes place. The green segment refers to the GEMC estimate $\xi_{LP} = 0.025(5)$ for $\lambda = 1.5$ and $\kappa = 4$ [24].

regime is attained, where stronger and stronger microphase or macrophase inhomogeneities progressively develop in the fluid. In Figs. 3 and 7, the quality of HNC predictions closely above such limiting temperatures can be directly appraised.

It is clear that good structural predictions will not guarantee equally accurate thermodynamic properties by the HNC theory. Just to quote a noteworthy example, for the square-well fluid with $\lambda = 1.5\sigma$ it was shown in Ref. [72] that a good agreement between HNC and MC is only obtained for the heat capacity, whereas the HNC pressures and internal energies show discrepancies with simulation results. Presumably, similar errors would also affect the determination of phase equilibria. Moreover, the lack of thermodynamic consistency introduces another source of ambiguity since different routes from structure to thermodynamics could be followed, leading in principle to different outcomes with different levels of accuracy. Therefore, in common with the conclusions of previous studies on different SALR fluids [11,34,43–53], the use of more sophisticated IET, such as the SCOZA or HMSA [37], might prove more suitable for an accurate determination of thermodynamic properties and phase equilibria in the SWLR model.

Both RPA schemes turn out to be comparatively less accurate; in particular, RPA-PY strongly underestimates the diverging trend of $S(q)$ at low temperatures, both in the case of clustering and liquid-vapor separation. In the latter case, RPA-ZC works slightly better. Using the RPA theory along with other approximations appropriate for low values of q , the Lifshitz point of the SWLR model can be determined analytically; this property is conveniently expressed in terms of the threshold value ξ_{LP} as a function of λ and κ . We find that both RPA schemes underestimate the minimum height of the repulsive barrier needed to induce microphase aggregation in the fluid. Since RPA-ZC returns ξ_{LP} values that are systematically larger than RPA-PY values, the former scheme performs slightly better. Even so, ξ values that are two to three times larger than predicted are required to induce clustering in the fluid.

We wish to comment about the possibility to model a real competing-interaction fluid in terms of SWLR interactions. With specific reference to our choices of $[\lambda, \kappa]$, type-II parametrizations [14] were the subject of a few experimental studies, involving charged PMMA particles [73,74], whereas no similar studies exist for type-III models. Changing the κ length in Eq. (1) so as to get a substantially shorter repulsive barrier, while keeping an equally short attractive well (type-I interaction), would make the SWLR potential more suitable to represent real colloidal suspensions [14]. On the other hand, we reiterate that in our opinion the great advantage of the SWLR interaction lies in its schematic, piecewise shape, which makes this model an ideal test bed for studying the separate effects of attraction and repulsion on the aggregation process in SALR fluids. At the same time, this peculiar property may be thought detrimental to represent real soft materials; as an example, a Yukawa long-range repulsion correctly describes the screened electrostatic forces acting in charged solutions. Indeed, two-Yukawa and Lennard-Jones-Yukawa SALR fluids have proved able to describe lysozyme

solutions (see, e.g., [4,5]) and charged colloidal suspensions (see, e.g., [1]).

We conclude by summarizing the highlights of this work: we have determined by MC simulations the structural portrait of the SWLR fluid, a model fluid which is attracting growing interest as a prototype system with competing interactions [24,56,60–66]. Gratifyingly, the HNC theory pinpoints with great accuracy a delicate crossover in the behavior of the model, such as the one between macrophase and microphase separation. The less sophisticated RPA theory, even when augmented with some reasonable prescription for the direct correlation function in the core region, works less accurately.

In a forthcoming study, we plan to analyze more closely, this time exclusively in terms of MC simulations, the SWLR fluid for values of ξ slightly above the Lifshitz point, in order to better characterize in this situation the shape and structure of the clusters.

ACKNOWLEDGMENT

This work has been done using the computer facilities made available by the PO-FESR 2007-2013 Project MedNETNA (Mediterranean Network for Emerging Nanomaterials).

APPENDIX A: THE RPA STRUCTURE FACTOR

In this Appendix we provide the straightforward derivation of the structure factor within the RPA theory. With specific reference to RPA-PY, Eq. (4), the reciprocal of the structure factor in Eq. (3) can be written as

$$\begin{aligned} \frac{1}{S(q)} &= 1 - \rho c_{HS}(q) + \rho \beta V_{SWLR}(q) \\ &= 1 - \rho c_{HS}(q) + \rho \beta [V_{SW}(q) + V_{LR}(q)], \end{aligned} \quad (A1)$$

where, for later convenience, the Fourier transform of the potential $V_{SWLR}(q)$ is written as the sum of the Fourier transforms of square-well and linear-ramp contributions $V_{SW}(q)$ and $V_{LR}(q)$, where

$$\begin{aligned} \frac{V_{SW}(r)}{\varepsilon} &= \begin{cases} -1, & 1 \leq r < \lambda \\ 0, & r \geq \lambda \end{cases} \quad \text{and} \\ \frac{V_{LR}(r)}{\varepsilon} &= \begin{cases} \xi(\kappa - r), & \lambda \leq r < \kappa \\ 0, & r \geq \kappa. \end{cases} \end{aligned} \quad (A2)$$

We recall that the Fourier transform of a spherically symmetric function $f(r)$ takes the form

$$f(q) = \frac{4\pi}{q} \int_0^\infty f(r) \sin(qr) r dr. \quad (A3)$$

As for the Percus-Yevick direct correlation function of hard spheres $c_{HS}(r)$, this is zero outside the core, whereas inside the core it is given by [25]

$$c_{HS}(r) = -A - Br - Cr^3 \quad (r < 1), \quad (A4)$$

where A , B , and C are certain functions of the packing fraction $\eta = \pi/6\rho\sigma^3$:

$$\begin{aligned} A &= \frac{(1+2\eta)^2}{(1-\eta)^4}, \\ B &= -6\eta \frac{(1+\eta/2)^2}{(1-\eta)^4}, \\ C &= \frac{\eta}{2} \frac{(1+2\eta)^2}{(1-\eta)^4}. \end{aligned} \quad (\text{A5})$$

Hence, in q space we get

$$c_{\text{HS}}(q) = -AJ_1(q) - BJ_2(q) - CJ_3(q) \quad (\text{A6})$$

with

$$J_1(q) = \frac{4\pi}{q} \int_0^1 r \sin(qr) dr = 4\pi \frac{\sin(q) - q \cos(q)}{q^3}, \quad (\text{A7a})$$

$$\begin{aligned} J_2(q) &= \frac{4\pi}{q} \int_0^1 r^2 \sin(qr) dr \\ &= 4\pi \frac{2q \sin(q) - (q^2 - 2) \cos(q) - 2}{q^4}, \end{aligned} \quad (\text{A7b})$$

$$\begin{aligned} J_3(q) &= \frac{4\pi}{q} \int_0^1 r^4 \sin(qr) dr \\ &= 4\pi \frac{(4q^3 - 24q) \sin(q) - (q^4 - 12q^2 + 24) \cos(q) + 24}{q^6}. \end{aligned} \quad (\text{A7c})$$

Still within RPA-PY, the Fourier transform of $V_{\text{SW}}(r)$ is given by

$$\begin{aligned} V_{\text{SW}}(q) &= -\frac{4\pi}{q} \int_1^\lambda r \sin(qr) dr \\ &= -4\pi \frac{\sin(q\lambda) - q\lambda \cos(q\lambda)}{q^3} \\ &\quad + \boxed{4\pi \frac{\sin(q) - q \cos(q)}{q^3}}. \end{aligned} \quad (\text{A8})$$

The boxed formula should be cut out when RPA-ZC is considered, since $V_{\text{SW}}(q)$ is now an integral extended from 0 to λ ; in this case, we exactly recover Eq. (24) of Ref. [24], but for a typo present therein, consisting in a change of sign (from minus to plus) in the first fraction.

As for the last term in Eq. (A1), we get

$$\begin{aligned} V_{\text{LR}}(q) &= \frac{4\pi}{q} \xi \kappa \int_\lambda^\kappa r \sin(qr) dr - \frac{4\pi}{q} \xi \int_\lambda^\kappa r^2 \sin(qr) dr \\ &= 4\pi \xi \kappa \frac{\sin(q\kappa)}{q^3} - 4\pi \xi \kappa \frac{\sin(q\lambda) - q\lambda \cos(q\lambda)}{q^3} \\ &\quad - 4\pi \xi \frac{2q\kappa \sin(q\kappa) + 2 \cos(q\kappa)}{q^4} \\ &\quad + 4\pi \xi \frac{2q\lambda \sin(q\lambda) - [(q\lambda)^2 - 2] \cos(q\lambda)}{q^4}. \end{aligned} \quad (\text{A9})$$

Upon plugging Eqs. (A6), (A8), and (A9) in Eq. (A1) we finally obtain the full analytical expression of $S(q)$.

The isothermal compressibility χ_T can be recovered from the $q \rightarrow 0$ limit of $S(q)$:

$$\rho k_B T \chi_T = S(0) = \lim_{q \rightarrow 0} \frac{1}{1 - \rho c_{\text{HS}}(q) + \rho \beta [V_{\text{SW}}(q) + V_{\text{LR}}(q)]}. \quad (\text{A10})$$

From Eqs. (A6) and (A7), we get

$$c_{\text{HS}}(0) = -\frac{4}{3}\pi A - \pi B - \frac{2}{3}\pi C = \frac{\pi}{6} \frac{\eta^3 - 4\eta^2 + 2\eta - 8}{(1-\eta)^4}, \quad (\text{A11})$$

or, in terms of the density,

$$c_{\text{HS}}(0) = \pi \frac{(\pi\rho)^3 - 24(\pi\rho)^2 + 72\pi\rho - 1728}{(6 - \pi\rho)^4}. \quad (\text{A12})$$

The above expression corrects the one provided in the first line of Eq. (25)b in Ref. [24]. As for the SWLR contribution, from Eqs. (A8) and (A9) we get

$$V_{\text{SWLR}}(0) = -\frac{4}{3}\pi (\lambda^3 - 1) + \frac{4}{3}\pi \xi \kappa (\kappa^3 - \lambda^3) - \pi \xi (\kappa^4 - \lambda^4), \quad (\text{A13})$$

where the first term on the right-hand side derives from the SW contribution and the other two terms from the LR contribution. With the aid of Eqs. (A11) and (A13), the reduced compressibility (A10) is completely determined. Should RPA-ZC be adopted instead, the constant term $(4/3)\pi$ is canceled; the sign inversion in [24] also affects the term $-(4/3)\pi\lambda^3$ in Eq. (A13) [see the second line of Eq. (25)b in [24]].

APPENDIX B: LIFSHITZ POINT WITHIN RPA

Following a common practice (see, e.g., [38,75]), we seek the maximum of $S(q)$ by finding the minimum of $c(q)$, and therefore we solve

$$\frac{dc(q)}{dq} = 0. \quad (\text{B1})$$

Now, in the low- q range we are interested in, $V_{\text{SW}}(q) + V_{\text{LR}}(q)$ in Eq. (A1) varies more rapidly than the hard-sphere contribution $c_{\text{HS}}(q)$. Therefore, we can reasonably neglect the derivative of $c_{\text{HS}}(q)$ and look for the solution to

$$\frac{d[V_{\text{SW}}(q) + V_{\text{LR}}(q)]}{dq} = 0. \quad (\text{B2})$$

Within this approximation, the Lifshitz point will neither depend on the temperature nor on the density, and is thus defined only in terms of the parameters of the SWLR interaction potentials λ , κ , and ξ .

As a further approximation, since we are interested in the low- q regime we can replace

$$\frac{\sin(qr)}{qr} \approx 1 - \frac{q^2 r^2}{6}, \quad (\text{B3})$$

and Eq. (A3) becomes

$$f(q) \approx f(0) - \frac{2\pi}{3} q^2 \int_0^\infty f(r) r^4 dr. \quad (\text{B4})$$

For the SWLR part in Eq. (B2), we then obtain

$$\begin{aligned}
 V_{\text{SW}}(q) + V_{\text{LR}}(q) &\approx V_{\text{SWLR}}(0) \\
 &- \frac{2\pi}{3} q^2 \int_1^\kappa [V_{\text{SW}}(q) + V_{\text{LR}}(q)] r^4 dr \\
 &= V_{\text{SWLR}}(0) \\
 &+ \pi q^2 \frac{6(\lambda^5 - 1) - 6\xi\kappa(\kappa^5 - \lambda^5) + 5\xi(\kappa^6 - \lambda^6)}{45}, \quad (\text{B5})
 \end{aligned}$$

where $V_{\text{SWLR}}(0)$ is given by Eq. (A13).

The expression (B5) is a parabola, $V_{\text{SWLR}}(0) + Aq^2$. When A is negative, the parabola is concave down and its maximum (at the vertex) falls at $q = 0$; correspondingly, $S(q)$ displays a minimum at the origin, and a maximum is therefore expected at $q_p > 0$, signaling microphase separation; in this case the fluid is above its Lifshitz point ξ_{LP} . In the opposite case $A > 0$,

the fluid exhibits liquid-vapor separation, i.e., it falls below its Lifshitz point. The threshold condition is realized when the fraction in Eq. (B5) vanishes, namely, for $\xi \equiv \xi_{\text{LP}}$ with

$$\xi_{\text{LP}}^{\text{PY}} = \frac{6(\lambda^5 - 1)}{\kappa^6 - 6\kappa\lambda^5 + 5\lambda^6}, \quad (\text{B6})$$

where the superscript PY indicates that this result holds for RPA-PY. Should RPA-ZC be employed, the (-1) term in the numerator of (B6) is canceled and the Lifshitz point becomes

$$\xi_{\text{LP}}^{\text{ZC}} = \frac{6\lambda^5}{\kappa^6 - 6\kappa\lambda^5 + 5\lambda^6}. \quad (\text{B7})$$

Clearly, if the long-range repulsion is switched off, i.e., $V_{\text{LR}}(r) = 0$, then the value of A , reducing to $6\pi(\lambda^5 - 1)/45$ in (B5), is always positive, as we would expect for a simple fluid, and in this case only liquid-vapor separation can occur.

-
- [1] F. Sciortino, P. Tartaglia, and E. Zaccarelli, *J. Phys. Chem. B* **109**, 21942 (2005).
- [2] F. Lo Verso, C. N. Likos, and L. Reatto, in *Smart Colloidal Materials*, edited by W. Richtering (Springer, Berlin, 2006), pp. 78–87.
- [3] J. J. McManus, A. Lomakin, M. Basan, A. Pande, O. Ogun, J. Pande, and G. B. Benedek, *Proc. Natl. Acad. Sci. USA* **104**, 16856 (2007).
- [4] F. Cardinaux, A. Stradner, P. Schurtenberger, F. Sciortino, and E. Zaccarelli, *Europhys. Lett.* **77**, 48004 (2007).
- [5] Y. Liu, L. Porcar, J. Chen, W.-R. Chen, P. Falus, A. Faraone, E. Fratini, K. Hong, and P. Baglioni, *J. Phys. Chem. B* **115**, 7238 (2011).
- [6] A. Ciach, J. Pękalski, and W. T. Gózdź, *Soft Matter* **9**, 6301 (2013).
- [7] N. E. Valadez-Pérez, R. Castañeda-Priego, and Y. Liu, *RSC Adv.* **3**, 25110 (2013).
- [8] J. Riest and G. Nägele, *Soft Matter* **11**, 9273 (2015).
- [9] A. P. Santos, J. Pękalski, and A. Z. Panagiotopoulos, *Soft Matter* **13**, 8055 (2017).
- [10] N. E. Valadez-Pérez, Y. Liu, and R. Castañeda-Priego, *Front. Phys.* **9**, 637138 (2021).
- [11] D. Pini, G. Jialin, A. Parola, and L. Reatto, *Chem. Phys. Lett.* **327**, 209 (2000).
- [12] Y. Zhuang and P. Charbonneau, *J. Phys. Chem. B* **120**, 7775 (2016).
- [13] M. B. Sweatman and L. Lue, *Adv. Theory Simul.* **2**, 1900025 (2019).
- [14] Y. Liu and Y. Xi, *Curr. Opin. Colloid Interface Sci.* **39**, 123 (2019).
- [15] J. L. Bretonnet, *AIMS Mater. Sci.* **6**, 509 (2019).
- [16] J. Ruiz-Franco and E. Zaccarelli, *Annu. Rev. Condens. Matter Phys.* **12**, 51 (2021).
- [17] O. Patsahan, M. Litniewski, and A. Ciach, *Soft Matter* **17**, 2883 (2021).
- [18] J. Tan, N. D. Afify, C. A. Ferreiro-Rangel, X. Fan, and M. B. Sweatman, *J. Chem. Phys.* **154**, 074504 (2021).
- [19] G. Munaò, S. Prestipino, and D. Costa, *Phys. Chem. Chem. Phys.* **23**, 22661 (2021).
- [20] G. Munaò, S. Prestipino, J. M. Bomont, and D. Costa, *J. Phys. Chem. B* **126**, 2027 (2022).
- [21] G. Munaò, D. Costa, G. Malescio, J. M. Bomont, and S. Prestipino, *Soft Matter* **18**, 6453 (2022).
- [22] A. Stradner, H. Sedgwick, F. Cardinaux, W. C. Poon, S. U. Egelhaaf, and P. Schurtenberger, *Nature (London)* **432**, 492 (2004).
- [23] B. Lonetti, E. Fratini, S. H. Chen, and P. Baglioni, *Phys. Chem. Chem. Phys.* **6**, 1388 (2004).
- [24] Y. Zhuang and P. Charbonneau, *J. Phys. Chem. B* **120**, 6178 (2016).
- [25] J. P. Hansen and I. R. McDonald, *Theory of Simple Liquids*, 3rd ed. (Academic, New York, 2006).
- [26] F. Sciortino, S. Mossa, E. Zaccarelli, and P. Tartaglia, *Phys. Rev. Lett.* **93**, 055701 (2004).
- [27] P. D. Godfrin, R. Castañeda-Priego, Y. Liu, and N. Wagner, *J. Chem. Phys.* **139**, 154904 (2013).
- [28] P. D. Godfrin, N. E. Valadez-Perez, R. Castañeda-Priego, N. Wagner, and Y. Liu, *Soft Matter* **10**, 5061 (2014).
- [29] J.-P. Hansen and L. Verlet, *Phys. Rev.* **184**, 151 (1969).
- [30] R. B. Jadrich, J. A. Bollinger, K. P. Johnston, and T. M. Truskett, *Phys. Rev. E* **91**, 042312 (2015).
- [31] J. A. Bollinger and T. M. Truskett, *J. Chem. Phys.* **145**, 064902 (2016).
- [32] J.-M. Bomont, D. Costa, and J.-L. Bretonnet, *Phys. Chem. Chem. Phys.* **19**, 15247 (2017).
- [33] J.-M. Bomont, D. Costa, and J.-L. Bretonnet, *Phys. Chem. Chem. Phys.* **22**, 5355 (2020).
- [34] J.-M. Bomont, D. Costa, and J.-L. Bretonnet, *AIMS Mater. Sci.* **7**, 170 (2020).
- [35] C. Caccamo, *Phys. Rep.* **274**, 1 (1996).
- [36] J.-M. Bomont, *Recent Advances in the Field of Integral Equation Theories: Bridge Functions and Applications to Classical Fluids* (Wiley, Hoboken, NJ, 2008), Chap. 1, pp. 1–84.
- [37] G. Pellicane, L. L. Lee, and C. Caccamo, *Fluid Phase Equilib.* **521**, 112665 (2020).
- [38] R. P. Sear and W. Gelbart, *J. Chem. Phys.* **110**, 4582 (1999).

- [39] Y. Liu, W.-R. Chen, and S.-H. Chen, *J. Chem. Phys.* **122**, 044507 (2005).
- [40] M. Broccio, D. Costa, Y. Liu, and S.-H. Chen, *J. Chem. Phys.* **124**, 084501 (2006).
- [41] A. Loredano-Osti and R. Castañeda-Priego, *J. Nanofluids* **1**, 36 (2012).
- [42] J.-L. Bretonnet, J.-M. Bomont, and D. Costa, *J. Chem. Phys.* **149**, 234907 (2018).
- [43] I. Guillén-Escamilla, J. G. Mèndez-Bermundèz, J. C. Mixteco-Sánchez, and G. A. Mèndez-Maldonado, *Rev. Mex. Fis.* **68**, 050502 (2022).
- [44] D. Pini, A. Parola, and L. Reatto, *J. Phys.: Condens. Matter* **18**, S2305 (2006).
- [45] A. J. Archer, D. Pini, R. Evans, and L. Reatto, *J. Chem. Phys.* **126**, 014104 (2007).
- [46] I. Guillén-Escamilla, M. Chávez-Páez, and R. Castañeda-Priego, *J. Phys.: Condens. Matter* **19**, 086224 (2007).
- [47] L. L. Lee, M. C. Hara, S. J. Simon, F. S. Ramos, A. J. Winkle, and J.-M. Bomont, *J. Chem. Phys.* **132**, 074505 (2010).
- [48] J. M. Kim, R. Castañeda-Priego, Y. Liu, and N. J. Wagner, *J. Chem. Phys.* **134**, 064904 (2011).
- [49] D. Costa, C. Caccamo, J.-M. Bomont, and J.-L. Bretonnet, *Mol. Phys.* **109**, 2845 (2011).
- [50] J.-M. Bomont and D. Costa, *J. Chem. Phys.* **137**, 164901 (2012).
- [51] J.-M. Bomont, J.-L. Bretonnet, D. Costa, and J.-P. Hansen, *J. Chem. Phys.* **137**, 011101 (2012).
- [52] P. D. Godfrin, P. Falus, L. Porcar, K. Hong, S. D. Hudson, N. J. Wagner, and Y. Liu, *Soft Matter* **14**, 8570 (2018).
- [53] R. Perdomo-Pèrez, J. Martínez-Rivera, N. C. Palmero-Cruz, M. A. Sandoval-Puentes, J. S. Gallegos, E. Lázaro-Lázaro, N. E. Valadez-Perèz, A. Torres-Carbajal, and R. Castañeda-Priego, *J. Phys.: Condens. Matter* **34**, 144005 (2022).
- [54] A. J. Archer and N. B. Wilding, *Phys. Rev. E* **76**, 031501 (2007).
- [55] J.-M. Bomont, J.-L. Bretonnet, and D. Costa, *J. Chem. Phys.* **132**, 184508 (2010).
- [56] G. Cigala, D. Costa, J.-M. Bomont, and C. Caccamo, *Mol. Phys.* **113**, 2583 (2015).
- [57] J. M. Olais-Govea, L. López-Flores, J. B. Zepeda-López, and M. Medina-Noyola, *Sci. Rep.* **9**, 16445 (2019).
- [58] A. G. Carretas-Talamante, J. B. Zepeda-López, E. Lázaro-Lázaro, L. F. Elizondo-Aguilera, and M. Medina-Noyola, *J. Chem. Phys.* **158**, 064506 (2023).
- [59] E. Sanz, K. A. White, P. S. Clegg, and M. E. Cates, *Phys. Rev. Lett.* **103**, 255502 (2009).
- [60] Y. Zhuang, K. Zhang, and P. Charbonneau, *Phys. Rev. Lett.* **116**, 098301 (2016).
- [61] Y. Zhuang and P. Charbonneau, *J. Chem. Phys.* **147**, 091102 (2017).
- [62] Y. Hu and P. Charbonneau, *Soft Matter* **14**, 4101 (2018).
- [63] H. Serna, E. G. Noya, and W. T. Gózdź, *Langmuir* **35**, 702 (2019).
- [64] H. Serna, E. G. Noya, and W. T. Gózdź, *Soft Matter* **16**, 718 (2020).
- [65] H. Serna, E. G. Noya, and W. T. Gózdź, *J. Phys. Chem. B* **124**, 10567 (2020).
- [66] H. Serna, A. G. Meyra, E. G. Noya, and W. T. Gózdź, *J. Phys. Chem. B* **126**, 7059 (2022).
- [67] A. J. Archer, C. Ionescu, D. Pini, and L. Reatto, *J. Phys.: Condens. Matter* **20**, 415106 (2008).
- [68] L. Belloni, *J. Chem. Phys.* **98**, 8080 (1993).
- [69] M. G. Noro and D. Frenkel, *J. Chem. Phys.* **113**, 2941 (2000).
- [70] B. A. Linnik, R. B. Jadrich, and T. M. Truskett, *Soft Matter* **12**, 2663 (2016).
- [71] B. A. Linnik, S. Dutta, R. B. Jadrich, D. Milliron, and T. M. Truskett, *Soft Matter* **13**, 1335 (2017).
- [72] D. Henderson, W. G. Madden, and D. D. Fitts, *J. Chem. Phys.* **64**, 5026 (1976).
- [73] C. L. Klix, C. P. Royall, and H. Tanaka, *Phys. Rev. Lett.* **104**, 165702 (2010).
- [74] T. H. Zhang, J. Klok, R. Hans Tromp, J. Groenewold, and W. K. Kegel, *Soft Matter* **8**, 667 (2012).
- [75] A. J. Archer, *Phys. Rev. E* **78**, 031402 (2008).